

MV-WAM: Manifold-Aware World Action Model with Value Augmentation

Jintao Chen^{1,2,*}, Peidong Jia^{1,2,*},†, Qingpo Wu^{1,2,*}, Jiaming Liu², Mengfei Du²,
 Chun-Kai Fan^{1,2}, Xiaowei Chi^{1,2}, Hao Chen², Chengyu Bai^{1,2}, Zezhong Qian^{1,2},
 Hao Wang^{1,2}, Jiajun Cao^{1,2}, Weishi Mi², Xiaozhu Ju², Jian Tang², Shanghang Zhang¹,[✉]

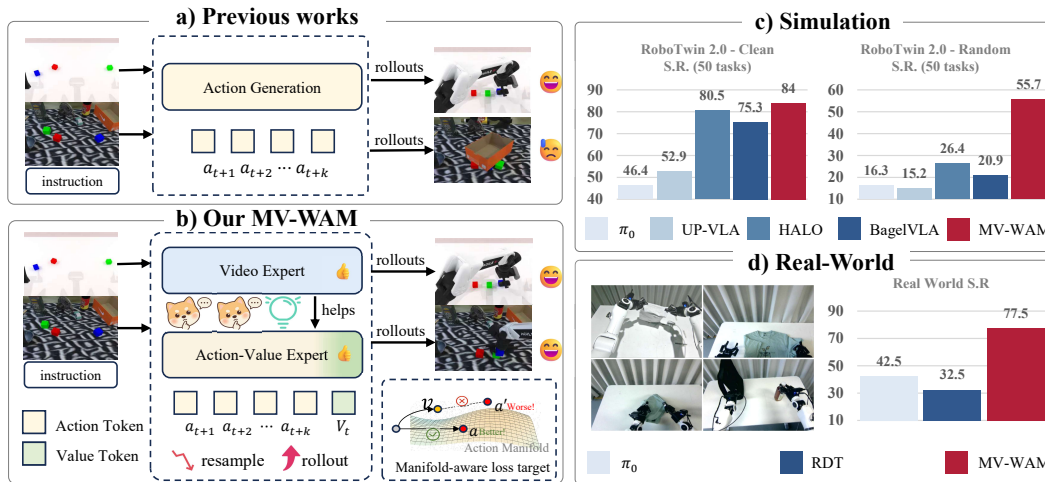


Figure 1: **Overview of MV-WAM.** We introduce asymmetric video-action experts with a causal mask to condition actions on visual dynamics. By coupling world modeling, action prediction, and progress-value estimation, it achieves strong performance in (c) simulation and (d) real-world tasks.

Abstract

Achieving robust and generalizable manipulation across diverse environments remains a fundamental challenge in embodied robotics. Recent world action models achieve strong in-domain performance, yet their gains do not extend proportionally to out-of-distribution scenarios. We attribute this to a structural mismatch between visual and action modalities, whose intrinsically heterogeneous manifolds cause joint optimization to disproportionately degrade action robustness under distribution shift. To address this, we propose **MV-WAM**, a novel end-to-end framework that jointly models visual prediction, action generation, and value estimation designed to effectively leverage video priors during both training and inference for enhanced action generalization. Key to this unification is a cross-modality causal mask that hierarchically grounds actions in predicted video frames and value function tokens in both modalities. To further narrow the generalization gap, MV-WAM adopts a manifold-aware optimization scheme that explicitly accounts for the structural heterogeneity across modalities. Finally, MV-WAM introduces a progress-value regulation mechanism that estimates task completion and detects misalignment between predicted frames and generated actions, enabling the policy to autonomously identify execution deviations and recover through value-guided rollback. On the RoboTwin simulation, MV-WAM achieves a **55.7%** mean success rate on random scenarios without any randomized action supervision, out-

*Equal Contribution. † Project Leader. ¹State Key Laboratory of Multimedia Information Processing, School of Computer Science, Peking University. ²Beijing Innovation Center of Humanoid Robotics. [✉] Corresponding author.

performing the strongest baseline by **29.3%**. MV-WAM achieves a **77.5%** mean success rate across four real-world tasks of varying difficulty on a dual-arm robot. Our results demonstrate that manifold-aware cross-modal alignment is essential for robust policy generalization, offering a path toward deployable robotic manipulation.

1 Introduction

Generalization is fundamental to deploying robotic manipulation policies in the real world [14]. Beyond the training distribution, policies must achieve visual generalization to unseen textures, lighting, backgrounds, and object configurations. Recent vision-language-action (VLA) models [5, 12, 25], built upon large-scale vision-language pretraining [32, 2, 1, 33], have substantially advanced manipulation policies in semantic and task-level generalization. However, this progress has not extended to visual and environmental generalization [14, 35], as policies trained on limited demonstrations cannot capture the visual diversity of real-world deployment. World Action Models (WAMs) extend the VLA paradigm by further leveraging large-scale action-free video data which captures far richer visual diversity than demonstration data alone [16, 15, 44], broadening visual generalization to regimes that curated demonstrations cannot reach. Yet realizing this promise has proven non-trivial.

Existing WAMs differ chiefly in how they integrate video prior into policies [3, 26, 44, 18, 46]. The most loose coupling is achieved by *decoupled* approaches, where a separate video model and policy interact only through generated visual predictions or latent representations [13, 42, 19, 37]. *Fully unified* approaches eliminate this distinction altogether, tokenizing visual and action signals into a single stream processed by shared transformer parameters [7, 49]. Approaches based on *Mixture-of-Transformers (MoTs)* [27] go further still, introducing modality-specific experts while sharing global attention, and currently achieve the strongest in-domain performance among WAM designs. Across these designs, all report consistent improvements over non-WAM baselines on in-domain and out-of-distribution (OOD) scenes alike. Despite these advances, as shown in Appendix D.1, in-domain performance steadily climbs while OOD gains lag behind, leaving a wide and in some cases growing generalization gap. Regardless of the architecture, the gains from video prior seem to flow disproportionately into visual prediction rather than action robustness, which is precisely what WAMs were designed to improve. Motivated by these observations, we aim to explore the following question: ***Why does deeper video-action coupling not translate to greater action generalization?***

We trace this gap to a manifold mismatch deeply embedded in current WAM architectures. Visual observations are high-dimensional and densely structured, governed by spatial and photometric regularities, whereas robot actions are low-dimensional, temporally structured, and precision-critical over control dimensions [5, 7]. These two modalities thus inhabit intrinsically heterogeneous representational manifolds [43]. Joint optimization over incompatible manifolds inevitably compromises action learning [45], leaving action representations under-trained and brittle. This is further aggravated by the sheer volume of visual tokens, which naturally dominates the shared objective. This misalignment is masked in-domain by strong cross-modal correlations, but under distribution shift, visual perturbations propagate through shared parameters and degrade action prediction [14]. This structural mismatch is architecture-agnostic, explaining why neither decoupled, fully unified, nor MoT-based designs have succeeded in closing the generalization gap.

As illustrated in Fig. 1, we propose **MV-WAM** (Manifold-Aware World Action Model with Value Augmentation), a novel framework that jointly generates future visual imaginations, robot actions, and value estimation within a unified architecture. At its core, MV-WAM adopts a MoTs backbone [27] in which each transformer layer hosts two modality-specific experts, one processing visual tokens and the other processing action-value tokens. Modality-specific experts share a global attention space while maintaining separate parameters. The visual expert is initialized from a large-scale pretrained video generative model [10], allowing MV-WAM to inherit a rich visual prior over physical dynamics, object interactions, and scene geometry that demonstration data alone cannot provide. Built on this framework, three principled components collectively enable action-free video to serve as a direct source of policy generalization. First, a *modality-adaptive optimization* scheme extends the plain MoTs into a manifold-aware multi-objective MoTs formulation, with each modality supervised according to the intrinsic structure of its target manifold. This eliminates cross-modal optimization interference and alleviates gradient imbalance, preventing each modality’s learning

signal from corrupting the other. Second, a *cross-modality causal mask* hierarchically routes information across modalities, grounding each action token in its corresponding predicted visual frame and each value token in both visual and action contexts, ensuring that action generation is always conditioned on the predicted visual future while preserving modality-specific structure. Third, a *progress-valued regulation* mechanism uses value tokens, trained with Monte Carlo task returns, to jointly estimate task progress and detect visual-action misalignment during execution. During online execution, when predicted values drop below a learned threshold, MV-WAM triggers a value-guided rollback, enabling the policy to autonomously identify and recover from execution deviations.

We evaluate MV-WAM extensively across simulation and real-world settings. On the RoboTwin 2.0 [8] benchmark, covering 50 manipulation tasks across both clean scenes and randomized scenes with perturbed lighting, backgrounds, and object configurations. MV-WAM achieves state-of-the-art performance under both settings, reaching a 55.7% success rate on unseen scenarios and outperforming the strongest baseline by 29.3% while matching its in-domain performance. On real-world dual-arm manipulation, MV-WAM further achieves 77.5% mean success rate across four tasks of varying difficulty, where baseline methods fail to generalize to physical deployment. Notably, MV-WAM achieves these gains with significantly fewer parameters than competing WAMs, suggesting that manifold-aware design rather than model scale is the key driver of generalization. Ablation studies further confirm that each architectural component contributes substantively to the OOD performance.

Our contributions are summarized as follows. **(1) MV-WAM framework.** We propose MV-WAM, a unified world action model built on MoTs that jointly generates visual predictions, robot actions, and value estimates, with a manifold-aware multi-objective formulation and a cross-modality causal mask that ground action generation in predicted visual futures while respecting the intrinsic geometry of each modality. **(2) Progress-valued regulation.** We introduce a progress-valued regulation mechanism that estimates task completion and detects visual-action misalignment, enabling autonomous deviation detection and value-guided recovery without human intervention. **(3) State-of-the-art generalization.** Extensive experiments on simulated and real-world manipulation tasks demonstrate state-of-the-art performance across in-domain, zero-shot, and few-shot settings.

2 Problem Definition and Analysis

2.1 Problem Formulation

We model robotic manipulation as a Partially Observable Markov Decision Process (POMDP) [23] $\langle \mathcal{S}, \mathcal{O}, \mathcal{A}, \mathcal{T}, \mathcal{L} \rangle$, where \mathcal{S} denotes the set of environment states, \mathcal{O} the set of visual observations, \mathcal{A} the action space, $\mathcal{T} : \mathcal{S} \times \mathcal{A} \rightarrow \Delta(\mathcal{S})$ the stochastic transition kernel, and \mathcal{L} the set of natural language task instructions. At each timestep t , the robot receives a task instruction $l \in \mathcal{L}$, perceives a history of visual observations $o_{t-h_O:t} \in \mathcal{O}^{h_O+1}$ as a partial observation of the underlying state $s_t \in \mathcal{S}$, and executes an action chunk $\mathbf{a}_{t:t+h_A} \in \mathcal{A}^{h_A+1} \subset \mathbb{R}^{h_A+1 \times d_a}$, where h_{A+1} is the action horizon and d_a is the action dimensionality. Upon completion of each action chunk, the robot observes the resulting environmental state and decides to either generate the next step or re-plan.

To solve the above POMDP problem, existing manipulation policies learn a parameterized mapping $\pi_\theta : \mathcal{O}^{h_O+1} \times \mathcal{L} \rightarrow \mathcal{A}$. As a common foundational scheme, Standard VLA models learn π_θ that maps historical observations and language instructions to action chunks, trained exclusively on action-paired demonstration data. WAMs extend this by incorporating abundant action-free video data as a visual prior, enabling π_θ to learn visual dynamics beyond paired demonstrations alone.

2.2 Preliminaries

We instantiate the action space \mathcal{A} following the unified action design of RDT-1B [30]. Each action $\mathbf{a}_t \in \mathbb{R}^{128}$ encodes both joint-level and end-effector control. Taking dual-arm robot as an example, this comprises 14-DoF relative joint offsets across the two arms and 2-DoF independent gripper states, standardized into the 128-dimensional representation for flexible and compatible manipulation.

Flow Matching We adopt conditional flow matching [28] as the generative backbone for both visual and action generation. Taking the action generation branch as an example, given a clean

target $\mathbf{a}_0 \in \mathcal{A}$, Gaussian noise $\mathbf{a}_1 \sim \mathcal{N}(\mathbf{0}, \mathbf{I})$ and diffusion timestep $\tau \in [0, 1]$, flow matching defines a linear interpolation $\mathbf{a}_\tau = (1 - \tau)\mathbf{a}_0 + \tau\mathbf{a}_1$ and trains the policy network π_θ to predict the vector field $\mathbf{v}_\theta(\mathbf{a}_\tau, \tau, \mathcal{C})$ conditioned on multi-modal context $\mathcal{C} = (\mathcal{O}^{h_o}, \mathcal{L}, \mathbf{s}_t)$ via:

$$\mathcal{L}_{\text{FM}} = \mathbb{E}_{\tau, \mathbf{a}_0, \mathbf{a}_1} \left\| \mathbf{v}_\theta(\mathbf{a}_\tau, \tau, \mathcal{C}) - (\mathbf{a}_1 - \mathbf{a}_0) \right\|_2^2. \quad (1)$$

At inference, the clean action chunk \mathbf{a}_0 is recovered by integrating \mathbf{v}_θ from \mathbf{a}_1 back to $\tau = 0$. Both the action branch and the video branch share the identical flow matching pipeline.

2.3 Manifold Analysis

We empirically verify that the generalization gap stems from an intrinsic manifold asymmetry between modalities. Existing WAMs exhibit a larger absolute clean-to-random gap than non-unified baselines (54.0–54.8 vs. 20.8–30.1 percentage drop), and t-SNE analysis confirms that action representations are significantly more sensitive to distribution shift than visual representations. Manifold curvature estimates reveal a consistent discrepancy ($\kappa_v = 3.8 \pm 0.6$ vs. $\kappa_a = 1.3 \pm 0.2$, $p < 0.001$), confirming that the two modalities inhabit incompatible manifolds. See Appendix D.1 for details.

We provide a formal analysis of why a manifold-agnostic optimization objective systematically loosens the generalization bound for the action modality. Following [34], for L -Lipschitz functions (π_θ here) on a compact Riemannian manifold with sectional curvature κ , the generalization error admits a curvature-dependent penalty $\psi(\kappa, L) = \sqrt{|\kappa|}/L$, which tightens only when the objective is geometrically matched to the target manifold. In existing unified WAMs, a single velocity-based objective calibrated to the high-curvature visual manifold \mathcal{M}_v is imposed on action modality. Since π_θ is jointly optimized over both manifolds, its Lipschitz regularity is governed by the more complex geometry of \mathcal{M}_v , effectively inflating the curvature experienced by the action branch from κ_a to κ_v . Since ψ is monotonically increasing in $|\kappa|$, this forces the action-side penalty to $\psi(\kappa_v, L) \gg \psi(\kappa_a, L)$, yielding a strictly looser bound on \mathcal{M}_a than a κ_a -matched objective would achieve. Under distribution shift, this looseness directly manifests as degraded action robustness, formally motivating our manifold-aware multi-objective formulation.

3 Method

3.1 Novel End-to-End Framework

To close the generalization gap arising from the structural mismatch between visual and action modalities, we propose a Manifold-Aware Unified Framework named **MV-WAM**, which unifies video world modeling, robotic action prediction, and value estimation within a single Transformer-based diffusion backbone. As illustrated in Fig. 2, our model is built upon stacked Diffusion Transformer (DiT) blocks comprising a Video Expert and an Action-Value Expert, coupled through a Mixture-of-Transformers (MoTs) [27] mechanism that enables cross-modal interaction. Rather than adopting the plain MoTs, we extend it into a manifold-aware multi-objective MoTs.

Dual Branch Expert architecture Both the Video Expert and Action-Value Expert adopt DiT backbones with identical depth and standard internal configurations. Task instructions \mathcal{L} are uniformly encoded via the umT5 [11] text encoder and injected into both experts through cross-attention. Specifically, the Video Expert is instantiated based on WoW-1.3B [10]. It first employs a spatiotemporal VAE to compress raw visual observation frames into compact latent representations, which are concatenated with mask tokens along the channel dimension, patched into visual tokens, and fed into the DiT backbone for video diffusion modeling. In contrast, the Action-Value Expert takes multi-view visual states \mathbf{s}_t encoded by SigLIP2 [38] as visual condition, with language embeddings injected into odd transformer layers and SigLIP2 visual embeddings into even layers. Within this expert, action tokens and state tokens share a unified encoder-decoder architecture for action generation, while value tokens are processed by an independent encoder-decoder for separate value estimation.

For precise temporal alignment during joint modeling, the Rotary Positional Embedding (RoPE) scaling factor of the Action-Value Expert is set to 1/4 of that used in the Video Expert. This synchronization establishes a unified temporal grid between action tokens and video latents, enabling

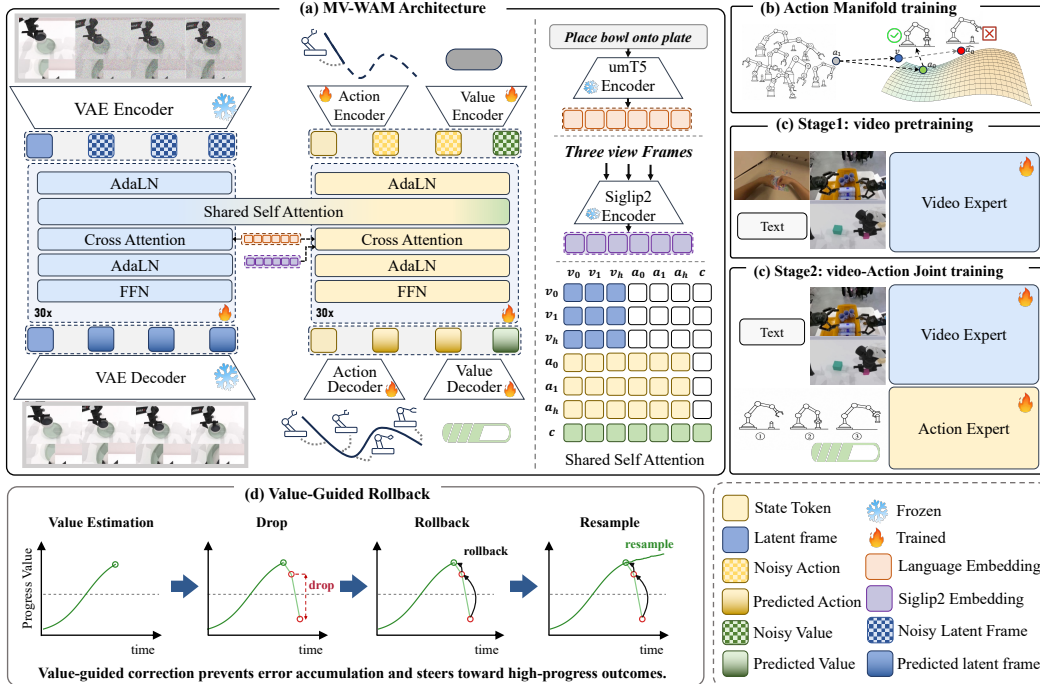


Figure 2: Overview of **MV-WAM**. (a) Detailed architecture comprises a Video Expert and an Action-Value Expert. (b) Manifold-aware Training. (c) Two-stage training, video-only pretraining followed by joint video-action training. (d) Value-guided rollback for online execution correction.

temporally coherent cross-modal interaction. We further adopt a structured causal attention mask to regulate information flow while preserving modality-specific priors. Video tokens are restricted to self-attention only within the visual stream to maintain high-fidelity video generation, whereas action and state tokens can attend to both video context and other action tokens. value tokens attend to visual, action, and state tokens jointly, enabling holistic assessment of task progress and visual-action alignment. This asymmetric masking ensures that action generation is always conditioned on visual predictions while video generation remains uncontaminated by action signals, and that value estimation has access to the full cross-modal context necessary for reliable task assessment.

Manifold-Aware Dual Prediction Objectives Instead of adopting a single unified diffusion objective for both modalities, we tailor two distinct manifold-aware prediction losses according to their intrinsic geometric properties. Visual and action data reside on Riemannian manifolds with significantly different curvatures, and optimizing both with one shared objective leads to severe geometric mismatch and suboptimal generalization. Our framework adopts separate flow-matching transformation functions for each branch. The Video Expert, defined on the high-curvature visual manifold, directly predicts the velocity field following standard flow matching:

$$\mathcal{L}_v = \mathbb{E}_{\tau, z_0, z_1} \|\pi_{\theta}^v(z_{\tau}, \tau, c) - (z_1 - z_0)\|_2^2, \quad (2)$$

where z_0 denotes clean video latents, z_1 is the noise prior, and $z_{\tau} = (1 - \tau)z_0 + \tau z_1$. π_{θ}^v and π_{θ}^a denote the Video Expert and Action-Value Expert respectively. For the Action-Value Expert, both action and value tokens reside on low-curvature manifolds with similar geometric structure. Using action as a representative example, the optimization objective is equivalent to directly regressing the clean action latent a_0 :

$$\mathcal{L}_a = \mathbb{E}_{\tau, a_0, a_1} \|\pi_{\theta}^a(a_{\tau}, \tau, c) - a_0\|_2^2. \quad (3)$$

The entire framework is jointly optimized by $\mathcal{L} = \lambda_v \mathcal{L}_v + \lambda_a \mathcal{L}_a$, where all balancing weights λ_v and λ_a are empirically set to 1. During inference, the Video Expert denoises latents from the predicted velocity field, while the Action-Value Expert directly outputs the optimized action representation. Benefiting from the manifold-aware dual objectives, MV-WAM simultaneously achieves high-fidelity visual world modeling and robust robotic action generation.

3.2 Progress-Valued Regulation

While manifold-aware objectives ensure geometric alignment during training, they provide no explicit signal to assess task progress or detect visual-action misalignment at inference time. In the absence of such feedback, execution deviations remain undetected and unrecoverable, directly undermining the policy’s generalization under distribution shift. To this end, we introduce a **Progress-Valued Regulation** mechanism that equips the Action-Value Expert with a dedicated value prediction capability, enabling the model to bias denoising trajectories toward high-progress outcomes.

Monte Carlo Value Estimation. Inspired by the paradigm of Cosmos Policy [24], we estimate the task value function c with Monte Carlo (MC) returns computed from executed trajectories. For each state-action pair in a trajectory, the value target is defined as the empirical discounted return accumulated from the current step t to the end of the trajectory:

$$\hat{c}(s_t, a_t) = \sum_{i=0}^{H-t} \gamma^i r(s_{t+i}, a_{t+i}), \tag{4}$$

where H is the trajectory horizon and γ is the discount factor (we set $\gamma = 0.99$). This MC target converts sparse task outcomes into a dense progress signal along the demonstration trajectory, serving as the supervision target for the value token.

Value-Guided Rollback for Online Execution. During closed-loop execution, the predicted value token serves as a dynamic progress monitor to detect and correct execution deviations in real-time. Specifically, we maintain a rolling buffer of recent state-Action-Value triplets and track the peak value $c_{\text{peak}} = \max_{i < t} \hat{c}_i$ achieved so far. At each control step, if the newly predicted value drops significantly below this peak (i.e., $\hat{c}_t < c_{\text{peak}} - \delta$, where δ is a task-aware threshold), the system flags the current action chunk as potentially erroneous. Upon triggering, the policy initiates a **rollback-and-resample** protocol: it reverts the execution state to the cached checkpoint corresponding to c_{peak} , effectively discarding the faulty action sequence. From this restored high-value state, the diffusion process is re-initialized to conditionally resample a new action chunk. Leveraging the inherent stochasticity of diffusion sampling, this correction can be performed efficiently without regenerating the entire trajectory or requiring additional environment queries. This value-triggered backtracking mechanism acts as a self-correcting loop that prevents error accumulation during long-horizon tasks, ensuring that the model consistently recovers from execution deviations and navigates toward high-progress regions of the action manifold.

4 Experiments

Training configuration is detailed in Section 4.1. We then benchmark MV-WAM against VLA and WAM baselines on RoboTwin 2.0 in Section 4.2, including zero-shot and few-shot generalization evaluations. Ablation studies in Section 4.3 validate our key design choices, followed by real-world evaluations in Section 4.4.

4.1 Training Configuration

Excluding the umT5 encoder and SigLIP2 encoder, the complete MV-WAM architecture contains 1.9B parameters. We construct a large-scale pre-training corpus by integrating diverse public robotic manipulation datasets covering a broad range of real-world scenarios, supplemented by egocentric data to strengthen the model’s visual understanding and spatial generalization. Detailed dataset statistics are provided in Appendix B. We perform a two-stage training procedure: we first pre-train the Video Expert on large-scale visual data, and then fine-tune the full model on paired demonstrations.

Video Expert pre-training. The Video Expert comprises 30 Transformer blocks and is initialized from WoW-1.3B [10], pre-trained for 20k steps with a batch size of 1024, a learning rate of 1×10^{-4} , and a weight decay of 1×10^{-2} using AdamW. Input videos are resized to 240×320 pixels.

Joint vision-action fine-tuning. The full model, comprising the pre-trained Video Expert and a 30-block Action-Value Expert trained from scratch, is fine-tuned for 15k steps with a batch size of

Table 1: **Results on the RoboTwin 2.0 benchmark (See Appendix G for details).** We evaluate models under both *Clean* and *Random* settings. Results report task-level manipulation success rates (%). † denotes reproduced using the official codebase. Mean SR denotes the average success rate.

Models	Adjust Bottle		Beat Block Hammer		Blocks Ranking RGB		Blocks Ranking Size		...	Turn Switch		Mean SR	
	Clean	Rand.	Clean	Rand.	Clean	Rand.	Clean	Rand.		Clean	Rand.	Clean	Rand.
π_0 [4]	90	56	43	21	19	5	7	1	...	27	23	46.4	16.3
RDT [30]	81	75	77	37	3	0	0	0	...	35	15	34.5	13.7
UP-VLA [47]	100	17	66	16	38	0	21	0	...	43	26	52.9	15.2
DP [9]	97	0	42	0	0	0	1	0	...	36	1	28.0	0.6
HALO [36]	97	9	96	11	94	7	58	2	...	65	27	80.5	26.4
BagelVLA [21]	100	14	87	16	84	4	45	2	...	49	30	75.3	20.5
Fast-WAM† [46]	95	0	74	2	0	1	38	0	...	56	17	71.9	6.3
Ours	83	65	75	53	99	88	63	43	...	62	65	84.0	55.7

512, a learning rate of 1×10^{-4} , and an action chunk size of 32. To reduce parameter count and computational cost, the Action-Value Expert operates at a lower hidden dimension of 768 and is projected to the 1536-dimensional video-token space only inside shared self attention. We adopt a learning rate schedule that remains constant for the first 20% of steps and decays linearly to zero thereafter. The model achieves an inference speed of **17.9** actions per second on a single A800 GPU.

4.2 Simulation Experiments

Benchmark and Protocol. We evaluate our method on the RoboTwin 2.0 [8] benchmark using the Aloha AgileX dual-arm embodiment. For VLA baselines, we follow the standard single-stage fine-tuning protocol, training each model on 50 *Clean* expert demonstrations per task. For WAM baselines and MV-WAM, we follow the two-stage training protocol of BagelVLA [21]: the Video Expert is first pre-trained on a mixture of 50 *Clean* and 500 *Random* demonstrations per task, and the full model is then fine-tuned exclusively on *Clean* paired demonstrations with video weights initialized from the first stage. This decoupled design deliberately introduces a distribution shift between fine-tuning and evaluation, providing a controlled measure of each model’s generalization capability. All models are evaluated on 100 rollouts per task under both *Clean* and *Random* conditions.

Baselines. We compare MV-WAM against seven baselines spanning two categories. For VLA models, we evaluate against DP [9], π_0 [4], and RDT [30]. For WAMs, we benchmark against UP-VLA [47], BagelVLA [21], HALO [36], and Fast-WAM [46].

Results. As shown in Table 1, MV-WAM achieves state-of-the-art performance across all tasks under both evaluation conditions, attaining average success rates of **84.0%** and **55.7%** on *Clean* and *Random*, respectively. Among VLA baselines, π_0 performs strongest at 46.4% / 16.3%, suggesting that standard VLA methods struggle to generalize to unseen visual perturbations when visual and action representations are learned independently.

Comparing against WAM baselines further validates the importance of modality-aware cross-modal alignment. While HALO, BagelVLA, and Fast-WAM achieve strong *Clean* performance (80.5%, 75.3%, and 71.9%), their *Random* performance remains substantially lower (26.4%, 20.5%, and 6.3%), indicating that visual prediction alone does not sufficiently transfer to action-level robustness. MV-WAM surpasses the strongest WAM baseline, HALO, by 3.5% on *Clean* and 29.3% on *Random*, and outperforms Fast-WAM by 12.1% on *Clean* and 49.4% on *Random*. Moreover, MV-WAM shows a notably smaller relative drop from *Clean* to *Random* (33.7%) compared to HALO (67.2%), BagelVLA (72.8%), and Fast-WAM (91.2%), confirming that geometry-aware prediction targets yield substantially more robust representations under distribution shift.

Table 2: **Zero- and few-shot generalization on 10 unseen tasks.** We evaluate MV-WAM under both *Clean* and *Random* settings across 0-shot, 1-shot, 5-shot, and 10-shot conditions. Results report task-level manipulation success rates (%). Mean SR denotes the average success rate across 10 tasks.

Task	0-shot		1-shot		5-shot		10-shot	
	Clean	Rand.	Clean	Rand.	Clean	Rand.	Clean	Rand.
Blocks Ranking Size	48	50	52	62	56	77	63	69
Click Bell	96	93	99	100	98	99	100	99
Place Dual Shoes	0	0	26	20	22	36	22	38
Move Stapler Pad	26	25	21	25	47	38	30	30
Shake Bottle Horiz.	98	100	97	100	95	100	100	100
Pick Dual Bottles	60	82	14	9	89	74	86	70
Place A2B Right	68	61	86	70	87	79	91	83
Place Bread Skillet	30	13	28	26	82	67	81	73
Place Cans Plasticbox	50	68	72	77	92	95	98	96
Stack Blocks Three	80	48	78	74	94	92	100	88
Mean SR	55.6	54.0	57.3	56.3	76.2	75.7	77.1	74.6

Zero-Shot and Few-Shot Generalization. To evaluate the transferability of MV-WAM to unseen tasks, we conduct zero-shot and few-shot Out-of-Distribution (OOD) experiments on RoboTwin 2.0. MV-WAM is trained on 40 tasks (a mixture of 50 Clean and 500 Random demonstrations per task, totally 22000 demonstrations) and evaluated on 10 OOD tasks. In the zero-shot setting, no demonstrations from test tasks are provided during fine-tuning. In the few-shot setting, we supply 1, 5, or 10 demonstrations per unseen task and fine-tune accordingly.

As shown in Table 2, MV-WAM already achieves strong performance in the zero-shot setting (55.6% / 54.0% on *Clean* / *Random*), demonstrating generalization to novel tasks without any task-specific supervision. Performance improves substantially at 10-shot, reaching 77.1% on *Clean* and 74.6% on *Random*, confirming that MV-WAM provides a strong foundation for data-efficient generalization to unseen manipulation tasks.

4.3 Ablation Study

Manifold-Aware Prediction Targets. All configurations use the same training setting and are trained for 15k steps, with only the prediction target assignment changed. As shown in Figure 3(a), the optimal configuration assigns direct x_0 -prediction to the action branch and velocity prediction to the video branch, achieving 84.0% / 55.7% on *Clean* / *Random*. Both noise-pred and flow-pred baselines collapse substantially under *Random* conditions (15.0% and 6.0%), confirming that applying a single unified objective across modalities severely degrades action robustness under distribution shift. These results validate our core design premise: robot actions reside on a low-dimensional, smooth manifold where direct state regression provides a more stable training signal, while the higher-curvature visual manifold favors velocity-based prediction.

Denosing Steps. We analyze the effect of the number of shared denosing steps applied to both the Video Expert and Action-Value Expert on task performance. As shown in Figure 3(b), performance improves consistently with additional steps but the gains diminish rapidly: MV-WAM with 3 steps already recovers over 96% of the *Clean* performance attained at 5 steps, while reducing denosing cost by 40%. Even with a single step, MV-WAM maintains competitive success rates (66.5% / 36.4%), demonstrating that the jointly trained representations are robust to coarse denosing schedules. We adopt 5 denosing steps as our default throughout all experiments.

Progress-Value Tokens. We further isolate the contribution of the progress-value prediction branch and the sensitivity of the inference-time rollback threshold δ . As shown in Figure 3(c), value tokens consistently improve over the no-value baseline (83.4% / 54.5%) across all tested thresholds, confirming that the task-completion signal provides complementary supervisory information for policy learning. Performance varies only marginally across δ values; we adopt $\delta=0.20$ as our default (84.0% / 55.7%), indicating that the rollback mechanism is robust to this hyperparameter.

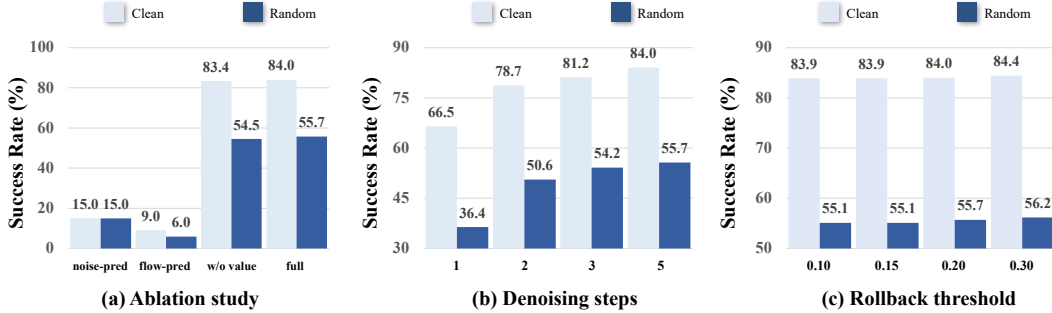


Figure 3: **Ablation study results.** (a) Manifold-aware prediction targets. (b) Effect of denoising steps. (c) Sensitivity to rollback threshold.

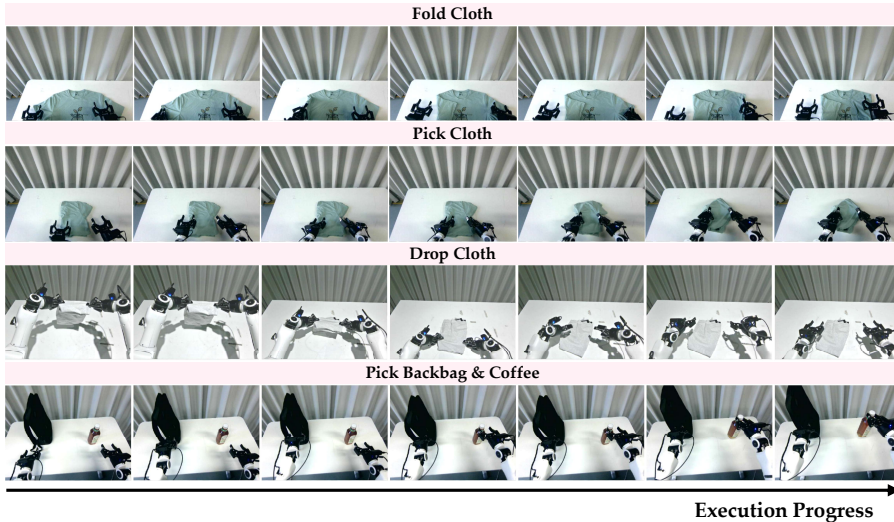


Figure 4: **Real-World Execution Visualization.** Execution progress across all four real-world manipulation tasks.

4.4 Real-World Experiments

Data Collection. To evaluate the practical applicability of MV-WAM, we deploy our framework on a TienKung dual-arm robot platform across four daily manipulation tasks of increasing difficulty: *Pick Backbag & Coffee*, *Drop Cloth*, *Pick Cloth*, and *Fold Cloth*, spanning rigid object grasping, cloth handling, and fine-grained deformable manipulation. We curate a dataset of 100 demonstrations per task, collected via human teleoperation at 30 FPS. Details of the hardware configuration and camera setup are provided in Appendix C.

Training and Evaluation Protocol. We train MV-WAM following the two-stage protocol described in Section 4.1, with three-view visual inputs from cameras mounted at the wrist and third-person perspectives of the TienKung platform. We compare against two representative baselines: (i) π_0 [4], a state-of-the-art generalist VLA model, and (ii) RDT [30], a large-scale diffusion-based robot foundation model. For fair comparison, all methods are initialized from their official pretrained checkpoints and fine-tuned with identical demonstration sets under full fine-tuning, then evaluated over 10 trials per task under varying object configurations.

Results. As shown in Table 3 and Figure 4, MV-WAM achieves the highest success rates across all four tasks, attaining a mean SR of **77.5%** and outperforming π_0 (42.5%) and RDT (32.5%) by substantial margins. On structured tasks such as *Drop Cloth* and *Pick Cloth*, MV-WAM achieves a perfect score of 100%, while both baselines fall below 70%, demonstrating that jointly trained visual-action representations yield more reliable rigid and semi-rigid manipulation. The gap is

Table 3: **Real-world experiment results on a TienKung robot.** We report success rates (%) over 10 trials per task.

Method	Pick Backbag	Drop Cloth	Pick Cloth	Fold Cloth	Mean SR
π_0 [4]	50	60	50	10	42.5
RDT [30]	30	40	60	0	32.5
MV-WAM (Ours)	90	100	100	20	77.5

most pronounced on *Fold Cloth*, the most demanding task requiring precise spatial reasoning and deformable object manipulation: MV-WAM achieves 20% compared to 10% for π_0 and 0% for RDT, confirming that geometry-aware cross-modal alignment is especially critical for fine-grained contact-rich tasks. Overall, these results demonstrate that the advantages of MV-WAM observed in simulation transfer effectively to physical deployment, and that grounding action generation in a jointly trained world model produces more robust manipulation policies across diverse real-world scenarios.

5 Conclusion

We presented MV-WAM, a unified world action model that jointly generates visual predictions, robot actions, and value estimates within a single MoTs-based diffusion backbone, while treating visual and action modalities as geometrically distinct through manifold-aware objectives and cross-modality causal masking. Experiments on RoboTwin 2.0 and real-robot platforms demonstrate that MV-WAM achieves state-of-the-art performance under both in-domain and OOD settings across simulation and physical deployment. These results suggest that closing the generalization gap requires not deeper integration, but more principled geometric alignment between modalities.

Limitations First, MV-WAM has not been validated at larger model scales, leaving the scalability of the proposed mechanisms an open question. Second, the Monte Carlo Value estimates may be noisy under sparse rewards, potentially limiting rollback reliability in long-horizon tasks.

References

- [1] Josh Achiam, Steven Adler, Sandhini Agarwal, Lama Ahmad, Ilge Akkaya, Florencia Leoni Aleman, Diogo Almeida, Janko Altenschmidt, Sam Altman, Shyamal Anadkat, et al. Gpt-4 technical report. *arXiv preprint arXiv:2303.08774*, 2023. 2
- [2] Jean-Baptiste Alayrac, Jeff Donahue, Pauline Luc, Antoine Miech, Iain Barr, Yana Hasson, Karel Lenc, Arthur Mensch, Katherine Millican, Malcolm Reynolds, et al. Flamingo: a visual language model for few-shot learning. *Advances in neural information processing systems*, 35:23716–23736, 2022. 2, 14
- [3] Hongzhe Bi, Hengkai Tan, Shenghao Xie, Zeyuan Wang, Shuhe Huang, Haitian Liu, Ruowen Zhao, Yao Feng, Chendong Xiang, Yinze Rong, et al. Motus: A unified latent action world model. *arXiv preprint arXiv:2512.13030*, 2025. 2, 14
- [4] Kevin Black, Noah Brown, Danny Driess, Adnan Esmail, Michael Equi, Chelsea Finn, et al. pi0: A vision-language-action flow model for general robot control. *arXiv preprint arXiv:2410.24164*, 2024. 7, 9, 10, 14, 18
- [5] Anthony Brohan, Noah Brown, Justice Carbajal, Yevgen Chebotar, Joseph Dabis, Chelsea Finn, Keerthana Gopalakrishnan, Karol Hausman, Alex Herzog, Jasmine Hsu, et al. Rt-1: Robotics transformer for real-world control at scale. *arXiv preprint arXiv:2212.06817*, 2022. 2, 14
- [6] Qingwen Bu, Jisong Cai, Li Chen, Xiuqi Cui, Yan Ding, Siyuan Feng, Shenyuan Gao, Xindong He, Xuan Hu, Xu Huang, et al. Agibot world colosseum: A large-scale manipulation platform for scalable and intelligent embodied systems. *arXiv preprint arXiv:2503.06669*, 2025. 14

- [7] Chi-Lam Cheang, Guangzeng Chen, Ya Jing, Tao Kong, Hang Li, Yifeng Li, Yuxiao Liu, Hongtao Wu, Jiafeng Xu, Yichu Yang, et al. Gr-2: A generative video-language-action model with web-scale knowledge for robot manipulation. *arXiv preprint arXiv:2410.06158*, 2024. 2
- [8] Tianxing Chen, Zanxin Chen, Baijun Chen, Zijian Cai, Yibin Liu, Zixuan Li, Qiwei Liang, Xianliang Lin, Yiheng Ge, Zhenyu Gu, et al. Robotwin 2.0: A scalable data generator and benchmark with strong domain randomization for robust bimanual robotic manipulation. *arXiv preprint arXiv:2506.18088*, 2025. 3, 7
- [9] Cheng Chi, Zhenjia Xu, Siyuan Feng, Eric Cousineau, Yilun Du, Benjamin Burchfiel, Russ Tedrake, and Shuran Song. Diffusion policy: Visuomotor policy learning via action diffusion. *The International Journal of Robotics Research*, 44(10-11):1684–1704, 2025. 7, 14, 18
- [10] Xiaowei Chi, Peidong Jia, Chun-Kai Fan, Xiaozhu Ju, Weishi Mi, Kevin Zhang, Zhiyuan Qin, Wanxin Tian, Kuangzhi Ge, Hao Li, et al. Wow: Towards a world omniscient world model through embodied interaction. *arXiv preprint arXiv:2509.22642*, 2025. 2, 4, 6
- [11] Hyung Won Chung, Noah Constant, Xavier Garcia, Adam Roberts, Yi Tay, Sharan Narang, and Orhan Firat. Unimax: Fairer and more effective language sampling for large-scale multilingual pretraining. In *International Conference on Learning Representations*, 2023. 4
- [12] Danny Driess, Fei Xia, Mehdi SM Sajjadi, Corey Lynch, Aakanksha Chowdhery, Brian Ichter, Ayzan Wahid, Jonathan Tompson, Quan Vuong, Tianhe Yu, et al. Palm-e: An embodied multimodal language model. *arXiv preprint arXiv:2303.03378*, 2023. 2, 14
- [13] Yilun Du, Sherry Yang, Bo Dai, Hanjun Dai, Ofir Nachum, Joshua B. Tenenbaum, Dale Schuurmans, and Pieter Abbeel. Learning universal policies via text-guided video generation. In *Advances in Neural Information Processing Systems (NeurIPS)*, 2023. 2
- [14] Jensen Gao, Suneel Belkhale, Sudeep Dasari, Ashwin Balakrishna, Dhruv Shah, and Dorsa Sadigh. A taxonomy for evaluating generalist robot manipulation policies. *IEEE Robotics and Automation Letters*, 2025. 2
- [15] David Ha and Jürgen Schmidhuber. World models. *arXiv preprint arXiv:1803.10122*, 2(3):440, 2018. 2
- [16] Danijar Hafner, Timothy Lillicrap, Jimmy Ba, and Mohammad Norouzi. Dream to control: Learning behaviors by latent imagination. *arXiv preprint arXiv:1912.01603*, 2019. 2
- [17] Ryan Hoque, Peide Huang, David J Yoon, Mouli Sivapurapu, and Jian Zhang. Egodex: Learning dexterous manipulation from large-scale egocentric video. *arXiv preprint arXiv:2505.11709*, 2025. 14
- [18] Junjun Hu, Jintao Chen, Haochen Bai, Minghua Luo, Shichao Xie, Ziyi Chen, Fei Liu, Zedong Chu, Xinda Xue, Botao Ren, et al. Astranav-world: World model for foresight control and consistency. *arXiv preprint arXiv:2512.21714*, 2025. 2
- [19] Yucheng Hu, Yanjiang Guo, Pengchao Wang, Xiaoyu Chen, Yen-Jen Wang, Jianke Zhang, Koushil Sreenath, Chaochao Lu, and Jianyu Chen. Video prediction policy: A generalist robot policy with predictive visual representations. *arXiv preprint arXiv:2412.14803*, 2024. 2
- [20] Yucheng Hu, Yanjiang Guo, Pengchao Wang, Xiaoyu Chen, Yen-Jen Wang, Jianke Zhang, Koushil Sreenath, Chaochao Lu, and Jianyu Chen. Video prediction policy: A generalist robot policy with predictive visual representations. *arXiv preprint arXiv:2412.14803*, 2024. 14
- [21] Yucheng Hu, Jianke Zhang, Yuanfei Luo, Yanjiang Guo, Xiaoyu Chen, Xinshu Sun, Kun Feng, Qingzhou Lu, Sheng Chen, Yangang Zhang, et al. Bagelvla: Enhancing long-horizon manipulation via interleaved vision-language-action generation. *arXiv preprint arXiv:2602.09849*, 2026. 7, 14, 18
- [22] Physical Intelligence, Kevin Black, Noah Brown, James Darpinian, Karan Dhabalia, Danny Driess, Adnan Esmail, Michael Equi, Chelsea Finn, et al. $\pi_{0.5}$: a vision-language-action model with open-world generalization, 2025. 14

- [23] Leslie Pack Kaelbling, Michael L Littman, and Anthony R Cassandra. Planning and acting in partially observable stochastic domains. *Artificial intelligence*, 101(1-2):99–134, 1998. 3
- [24] Moo Jin Kim, Yihuai Gao, Tsung-Yi Lin, Yen-Chen Lin, Yunhao Ge, Grace Lam, Percy Liang, Shuran Song, Ming-Yu Liu, Chelsea Finn, et al. Cosmos policy: Fine-tuning video models for visuomotor control and planning. *arXiv preprint arXiv:2601.16163*, 2026. 6
- [25] Moo Jin Kim, Karl Pertsch, Siddharth Karamcheti, Ted Xiao, Ashwin Balakrishna, Suraj Nair, Rafael Rafailov, Ethan Foster, Grace Lam, Pannag Sanketi, et al. Openvla: An open-source vision-language-action model. *arXiv preprint arXiv:2406.09246*, 2024. 2, 14
- [26] Lin Li, Qihang Zhang, Yiming Luo, Shuai Yang, Ruilin Wang, Fei Han, Mingrui Yu, Zelin Gao, Nan Xue, Xing Zhu, et al. Causal world modeling for robot control. *arXiv preprint arXiv:2601.21998*, 2026. 2
- [27] Weixin Liang, Lili Yu, Liang Luo, Srinivasan Iyer, Ning Dong, Chunting Zhou, Gargi Ghosh, Mike Lewis, Wen-tau Yih, Luke Zettlemoyer, et al. Mixture-of-transformers: A sparse and scalable architecture for multi-modal foundation models. *arXiv preprint arXiv:2411.04996*, 2024. 2, 4, 14
- [28] Yaron Lipman, Ricky TQ Chen, Heli Ben-Hamu, Maximilian Nickel, and Matt Le. Flow matching for generative modeling. *arXiv preprint arXiv:2210.02747*, 2022. 3
- [29] Jiaming Liu, Hao Chen, Pengju An, Zhuoyang Liu, Renrui Zhang, Chenyang Gu, Xiaoqi Li, Ziyu Guo, Sixiang Chen, Mengzhen Liu, et al. Hybridvla: Collaborative diffusion and autoregression in a unified vision-language-action model. *ICLR*, 2025. 14
- [30] Songming Liu, Lingxuan Wu, Bangguo Li, Hengkai Tan, Huayu Chen, Zhengyi Wang, Ke Xu, Hang Su, and Jun Zhu. Rdt-1b: a diffusion foundation model for bimanual manipulation. *arXiv preprint arXiv:2410.07864*, 2024. 3, 7, 9, 10, 18
- [31] Abby O’Neill, Abdul Rehman, Abhiram Maddukuri, Abhishek Gupta, Abhishek Padalkar, Abraham Lee, Acorn Pooley, Agrim Gupta, Ajay Mandlekar, Ajinkya Jain, et al. Open x-embodiment: Robotic learning datasets and rt-x models: Open x-embodiment collaboration 0. In *2024 IEEE International Conference on Robotics and Automation (ICRA)*, pages 6892–6903. IEEE, 2024. 14
- [32] Alec Radford, Jong Wook Kim, Chris Hallacy, Aditya Ramesh, Gabriel Goh, Sandhini Agarwal, Girish Sastry, Amanda Askell, Pamela Mishkin, Jack Clark, et al. Learning transferable visual models from natural language supervision. In *International conference on machine learning*, pages 8748–8763. PmlR, 2021. 2, 14
- [33] Alec Radford, Jong Wook Kim, Chris Hallacy, Aditya Ramesh, Gabriel Goh, Sandhini Agarwal, Girish Sastry, Amanda Askell, Pamela Mishkin, Jack Clark, Gretchen Krueger, and Ilya Sutskever. Learning transferable visual models from natural language supervision. In *ICML*, pages 8748–8763, 2021. 2
- [34] Krisanu Sarkar. Learning beyond euclid: Curvature-adaptive generalization for neural networks on manifolds. *arXiv preprint arXiv:2507.02999*, 2025. 4, 17
- [35] Xiaofeng Shi, Zhenjia Xu, Zhiyuan Wang, and Katerina Fragkiadaki. Learning generalizable manipulation policies with object-centric 3d representations. In *Conference on Robot Learning*, 2023. 2
- [36] Quanxin Shou, Fangqi Zhu, Shawn Chen, Puxin Yan, Zhengyang Yan, Yikun Miao, Xiaoyi Pang, Zicong Hong, Ruikai Shi, Hao Huang, et al. Halo: A unified vision-language-action model for embodied multimodal chain-of-thought reasoning. *arXiv preprint arXiv:2602.21157*, 2026. 7, 14, 18
- [37] Yang Tian, Sizhe Yang, Jia Zeng, Ping Wang, Dahua Lin, Hao Dong, and Jiangmiao Pang. Predictive inverse dynamics models are scalable learners for robotic manipulation. *arXiv preprint arXiv:2412.15109*, 2024. 2

- [38] Michael Tschannen, Alexey Gritsenko, Xiao Wang, Muhammad Ferjad Naeem, Ibrahim Al-abdulmohsin, Nikhil Parthasarathy, Talfan Evans, Lucas Beyer, Ye Xia, Basil Mustafa, Olivier Hénaff, Jeremiah Harmsen, Andreas Steiner, and Xiaohua Zhai. Siglip 2: Multilingual vision-language encoders with improved semantic understanding, localization, and dense features. *arXiv preprint arXiv:2502.14786*, 2025. 4
- [39] Junjie Wen, Minjie Zhu, Yichen Zhu, Zhibin Tang, Jinming Li, Zhongyi Zhou, Chengmeng Li, Xiaoyu Liu, Yaxin Peng, Chaomin Shen, et al. Diffusion-vla: Scaling robot foundation models via unified diffusion and autoregression. *arXiv preprint arXiv:2412.03293*, 2024. 14
- [40] Kun Wu, Chengkai Hou, Jiaming Liu, Zhengping Che, Xiaozhu Ju, Zhuqin Yang, Meng Li, Yinuo Zhao, Zhiyuan Xu, Guang Yang, et al. Robomind: Benchmark on multi-embodiment intelligence normative data for robot manipulation. *arXiv preprint arXiv:2412.13877*, 2024. 14
- [41] Shihan Wu, Xuecheng Liu, Shaoxuan Xie, Pengwei Wang, Xinghang Li, Bowen Yang, Zhe Li, Kai Zhu, Hongyu Wu, Yiheng Liu, et al. Robocoin: An open-sourced bimanual robotic data collection for integrated manipulation. *arXiv preprint arXiv:2511.17441*, 2025. 14
- [42] Sherry Yang, Yilun Du, Kamyar Ghasemipour, Jonathan Tompson, Dale Schuurmans, and Pieter Abbeel. Learning interactive real-world simulators. In *International Conference on Learning Representations (ICLR)*, 2024. 2
- [43] Yandan Yang, Shuang Zeng, Tong Lin, Xinyuan Chang, Dekang Qi, Junjin Xiao, Haoyun Liu, Ronghan Chen, Yuzhi Chen, Dongjie Huo, et al. Abot-m0: Vla foundation model for robotic manipulation with action manifold learning. *arXiv preprint arXiv:2602.11236*, 2026. 2
- [44] Seonghyeon Ye, Yunhao Ge, Kaiyuan Zheng, Shenyuan Gao, Sihyun Yu, George Kurian, Suneel Indupuru, You Liang Tan, Chuning Zhu, Jiannan Xiang, et al. World action models are zero-shot policies. *arXiv preprint arXiv:2602.15922*, 2026. 2
- [45] Tianhe Yu, Saurabh Kumar, Abhishek Gupta, Sergey Levine, Karol Hausman, and Chelsea Finn. Gradient surgery for multi-task learning. In *Advances in Neural Information Processing Systems*, volume 33, pages 5824–5836, 2020. 2
- [46] Tianyuan Yuan, Zibin Dong, Yicheng Liu, and Hang Zhao. Fast-wam: Do world action models need test-time future imagination? *arXiv preprint arXiv:2603.16666*, 2026. 2, 7, 14, 18
- [47] Jianke Zhang, Yanjiang Guo, Yucheng Hu, Xiaoyu Chen, Xiang Zhu, and Jianyu Chen. Up-vla: A unified understanding and prediction model for embodied agent. *arXiv preprint arXiv:2501.18867*, 2025. 7, 14, 18
- [48] Tony Z Zhao, Vikash Kumar, Sergey Levine, and Chelsea Finn. Learning fine-grained bimanual manipulation with low-cost hardware. *arXiv preprint arXiv:2304.13705*, 2023. 14
- [49] Fangqi Zhu, Hongtao Wu, Song Guo, Yuxiao Liu, Chilam Cheang, and Tao Kong. Irasim: Learning interactive real-robot action simulators. *arXiv preprint arXiv:2406.14540*, 2024. 2

A Related Work

Vision-Language-Action Models. Early imitation learning approaches such as ACT [48] and Diffusion Policy [9] demonstrated the effectiveness of expressive policy architectures for manipulation, but rely on task-specific designs that generalize poorly across diverse scenarios and unseen visual conditions. VLA models address this by leveraging pretrained vision-language models [32, 2] to parameterize manipulation policies, enabling natural language instruction following and broader semantic generalization. Several pioneering works [5, 12, 25] demonstrate that training on large-scale and diverse robot demonstration datasets can substantially enhance the cross-task generalization of VLA models. To capture more complex action distributions, subsequent works augment VLA policies with continuous generative heads, encompassing diffusion-based denoising formulations [39, 29] and flow-matching alternatives that enable more efficient continuous action synthesis [4, 22]. Despite these advances, VLA models remain brittle under environmental perturbations such as novel lighting, background textures, and unseen object configurations, as their visual representations are learned from demonstration corpora that cannot exhaustively cover real-world deployment diversity. MV-WAM addresses this limitation by incorporating a large-scale video-generative prior that broadens visual coverage well beyond what labeled demonstrations can provide.

World Action Models. A growing line of work seeks to improve policy generalization by incorporating world modeling into the action learning loop. UP-VLA [47] and Video Prediction Policy (VPP) [20] introduce visual prediction as an auxiliary objective to enrich visual representations, while BagelVLA [21] interleaves linguistic planning and visual forecasting sequentially before action generation. Fast-WAM [46] demonstrates that the primary benefit of world modeling lies in representation learning during training rather than explicit future imagination at inference time. More recent work such as Motus [3] and HALO [36] adopt Mixture-of-Transformers architectures [27] to unify understanding, visual prediction, and action generation within a single model, achieving strong performance on challenging manipulation benchmarks.

B Pre-training Dataset Details

We summarize the datasets used in our two-stage pre-training pipeline in Table 4. The corpus covers a broad range of real-world manipulation scenarios collected through both human demonstration and robot teleoperation, totaling approximately 7,500 hours of interaction data.

Table 4: **Datasets used in embodied data pre-training.** We list each dataset and its estimated data collection duration in hours.

Dataset	Hours
EgoDex [17]	800
Agibot [6]	2,500
RoboMind [40]	1,000
RoboCoin [41]	1,000
Open X-Embodiment [31]	2,000
Internal private data	200
Total	7,500

C Real-World Experiment Setup

C.1 TienKung Dual-Arm Robot Setup



Figure 5: **Real-world robot experiment setup.** The TienKung dual-arm platform with two wrist-mounted cameras and one stationary head camera for three-view RGB observation.

As shown in Figure 5, the physical deployment of MV-WAM utilizes a TienKung dual-arm robot platform designed for dexterous bimanual manipulation. The perceptual system consists of three Orbbec Gemini 330 RGB-D cameras: two wrist-mounted cameras providing close-range views of each end-effector for fine-grained contact reasoning, and one stationary third-person camera offering a global workspace perspective for spatial planning and task progress monitoring.

All demonstration trajectories were collected via human teleoperation at 30 FPS, with 300 high-quality demonstrations curated per task. We adopt a unified action space $\mathbf{a} \in \mathbb{R}^{16}$, where each of the two arms contributes 7-DoF joint position commands (delta angles) and 1-DoF gripper state:

$$\mathbf{a} = [\Delta\theta_{1:7}^R, g^R, \Delta\theta_{1:7}^L, g^L] \in \mathbb{R}^{16}. \quad (5)$$

During training, the three-view RGB observations are encoded by SigLIP2 as the visual condition input to the Action-Value Expert, following the same protocol described in Section 4.1. All methods are initialized from their official pretrained checkpoints and fine-tuned on the collected demonstrations under identical settings for fair comparison.

D Generalization Analysis in Unified World Action Models

D.1 The Generalization Gap Persists Across Architectures

The key distinction between VLAs and WAMs lies in whether visual state prediction and action generation are jointly optimized within a shared latent space. Unified models, including BagelVLA and HALO, achieve substantially higher success rates under clean conditions (75.3%–80.5%) compared to non-unified baselines (28.0%–46.4%). Yet a natural question arises: *does this shared latent space actually bridge the generalization gap?*

Empirical evidence suggests otherwise. All models are evaluated on RoboTwin 2.0, where training demonstrations consist

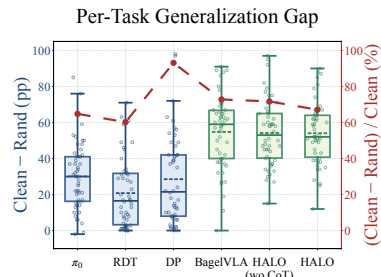


Figure 6: Generalization Gap for models.

exclusively of clean-condition action trajectories without any domain-randomized action supervision. As shown in Fig. 6, the gap retention rate $(\text{Clean} - \text{Random})/\text{Clean}$ remains consistently high across both unified and non-unified architectures, ranging from 60.2% to 93.1% for non-unified models and 67.1% to 72.8% for unified models. More critically, the absolute clean-to-random gap of unified models (54.0 to 54.8 percentage points) substantially exceeds that of non-unified baselines (20.8 to 30.1 percentage points), indicating that out-of-distribution robustness not only fails to improve but degrades in absolute terms. These results suggest that visual and action generalization remain largely decoupled even when optimized within a shared latent space, and that spatiotemporal priors acquired through visual prediction do not effectively transfer to action-level robustness under environmental perturbation.

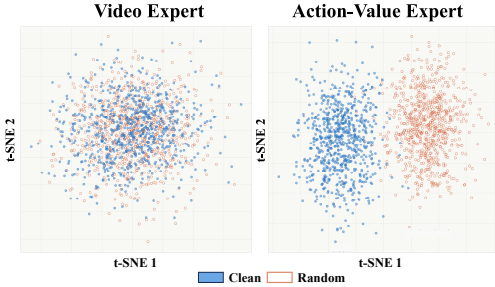


Figure 7: t-SNE visualization of visual and action expert representations after per-task mean centering. From inter-task variation, we apply per-task mean centering by subtracting the mean feature vector of each task before aggregating all samples for t-SNE visualization (perplexity = 50).

The t-SNE results reveal a clear representational asymmetry between the two experts as shown in Fig. 7. Visual expert features under clean and domain-randomized conditions remain largely intermingled, indicating that the visual representations are robust to environmental perturbation. In contrast, action expert features form two clearly separated clusters under the same perturbations, demonstrating that the action representations are significantly more sensitive to distributional shift. This asymmetry suggests that while unified modeling enables the visual latent space to generalize across conditions, this robustness does not propagate to the action latent space, confirming that visual and action generalization remain decoupled even within a shared latent space. ***Joint optimization in a shared latent space is necessary but not sufficient for generalization transfer across modalities.***

The representational asymmetry observed above naturally raises a deeper question: does this reflect an intrinsic difference in the underlying geometry of the two modalities? Manifold curvature at each sample point is estimated via the ratio of geodesic distance to Euclidean distance between each paired clean and randomized sample, where a higher ratio indicates greater local curvature. Since the visual observation space is high-dimensional, we first apply PCA to reduce each frame to 50 dimensions before constructing a 10-nearest-neighbor graph for geodesic distance approximation via shortest-path computation. For the action modality, curvature is computed directly in the native action space without dimensionality reduction, as the action vector is inherently low-dimensional. Per-task curvature estimates are obtained by averaging over all valid paired samples within each task, and statistical significance is assessed via the Mann-Whitney U test across the 50 tasks.

Table 5: Manifold curvature estimates for visual and action modalities across 50 tasks.

Modality	κ (mean \pm std)	p-value
Visual	3.8 ± 0.6	<0.001
Action	1.3 ± 0.2	

intrinsic rather than learned. This finding suggests that the failure of generalization transfer in unified models is not a training artifact, but a structural consequence of forcing two geometrically incompatible manifolds into a shared latent space under a single optimization objective.

We probe whether this failure stems from a fundamental asymmetry in how visual and action representations respond to distributional shift. Specifically, we extract features from both the visual and action experts at the shared self-attention layer. For each of the 50 tasks, we randomly sample 3 episodes and 5 frames per episode under both clean and domain-randomized conditions, regardless of task success, yielding approximately 750 points per condition. Since the number of tokens differs between the visual and action experts, we apply mean pooling over all tokens within each frame to obtain a fixed-dimensional representation per frame. To isolate condition-level variation we apply mean centering by subtracting the mean feature vector of each task before aggregating all samples for t-SNE visualization (perplexity = 50).

As shown in Table 5, the visual manifold exhibits significantly higher curvature than the action manifold across all 50 tasks, and this difference is consistent regardless of task type or perturbation condition. Critically, since this measurement is performed entirely in raw data space and is independent of any model or training procedure, it confirms that ***the geometric discrepancy between the two modalities is***

D.2 Manifold-Aware Optimization as a Necessary Condition

Building on the curvature discrepancy established above, we now provide a formal analysis of why a manifold-agnostic optimization objective systematically loosens the generalization bound for the action modality. While our empirical proxy (the geodesic-to-Euclidean distance ratio) is not a direct estimate of sectional curvature, the consistent ordering $\kappa_v \gg \kappa_a$ across all 50 tasks provides the structural foundation required for this analysis. Following [34], for a class of L -Lipschitz functions (here, the policy π_θ) on a compact Riemannian manifold with sectional curvature κ , the generalization error admits a curvature-dependent penalty $\psi(\kappa, L) = \sqrt{|\kappa|}/L$. Crucially, this bound tightens only when the optimization objective is geometrically matched to the target manifold’s intrinsic structure.

In existing unified models, a single velocity-based objective calibrated to the high-curvature visual manifold \mathcal{M}_v is imposed uniformly across modalities. Because π_θ is jointly optimized over both manifolds, its overall Lipschitz regularity is governed by the more complex geometry of \mathcal{M}_v . This shared parameterization effectively inflates the curvature experienced by the action branch from its native κ_a to κ_v . Since ψ is monotonically increasing in $|\kappa|$, this structural mismatch forces the action-side penalty to $\psi(\kappa_v, L) \gg \psi(\kappa_a, L)$, yielding a strictly looser bound on \mathcal{M}_a than a κ_a -matched objective would achieve. Under distributional shift, this looseness directly manifests as degraded action robustness, formally motivating our manifold-aware multi-objective formulation that independently matches each modality’s optimization to its intrinsic geometry.

E Algorithm

Continuous Flow Matching (CFM) defines a deterministic linear interpolation path between target data $x_0 \sim p_{\text{data}}$ and Gaussian noise $x_1 \sim \mathcal{N}(\mathbf{0}, \mathbf{I})$:

$$x_t = (1 - t)x_0 + tx_1, \quad t \in [0, 1]. \quad (6)$$

The three common prediction parameterizations differ only in the supervised target and in how the inference-time velocity is reconstructed from the model output. Table 6 summarizes these equivalent forms.

Table 6: Prediction parameterizations for continuous flow matching.

Parameterization	Model output	Training loss	Inference velocity
v -prediction	$\hat{v}_\theta(x_t, t)$	$\mathbb{E} \left[\ \hat{v}_\theta(x_t, t) - (x_1 - x_0)\ _2^2 \right]$	$v_\theta(x_t, t) = \hat{v}_\theta(x_t, t)$
x_0 -prediction	$\hat{x}_{0,\theta}(x_t, t)$	$\mathbb{E} \left[\ \hat{x}_{0,\theta}(x_t, t) - x_0\ _2^2 \right]$	$v_\theta(x_t, t) = x_1 - \hat{x}_{0,\theta}(x_t, t)$
Noise-prediction	$\hat{x}_{1,\theta}(x_t, t)$	$\mathbb{E} \left[\ \hat{x}_{1,\theta}(x_t, t) - x_1\ _2^2 \right]$	$v_\theta(x_t, t) = \frac{\hat{x}_{1,\theta}(x_t, t) - x_t}{1 - t}$

In practice, the denominators in the x_0 - and noise-prediction forms are clipped near the endpoints of the ODE trajectory for numerical stability.

F Discussion

Relation to prior x_0 -prediction methods. Although MV-WAM uses an x_0 -style target for the action branch, this design differs from prior endpoint-prediction formulations such as pixel Mean-Flow and Abot-M0. These methods predict a clean endpoint at the network-output level, but define supervision in the velocity space. Under our convention $x_t = (1 - t)x_0 + tx_1$, this yields

$$\left\| \frac{x_t - \hat{x}_{0,\theta}}{t} - \frac{x_t - x_0}{t} \right\|_2^2 = \frac{1}{t^2} \|\hat{x}_{0,\theta} - x_0\|_2^2, \quad (7)$$

which is an endpoint regression loss reweighted by $1/t^2$. This weighting is suitable when the objective is used as a single generative loss, because it emphasizes endpoint accuracy near the data side of the flow trajectory. In MV-WAM, however, action prediction is jointly optimized with video generation. Directly adopting the velocity-space x_0 loss would cause the action loss to diverge as

Table 7: **Results on the RoboTwin 2.0 benchmark.** We evaluate models under both clean and randomized settings. Results report task-level manipulation success rates (%). The last row reports the average success rate across all tasks.

Task	DP [9]		RDT [30]		π_0 [4]		UP-VLA [47]		BagelVLA [21]		HALO [36]		Fast-WAM [46]		Ours	
	Clean	Rand.	Clean	Rand.	Clean	Rand.	Clean	Rand.	Clean	Rand.	Clean	Rand.	Clean	Rand.	Clean	Rand.
Adjust Bottle	97	0	81	75	90	56	100	17	100	14	97	9	95	0	83	65
Beat Block Hammer	42	0	77	37	43	21	66	16	87	16	96	11	74	2	75	53
Blocks Ranking RGB	0	0	3	0	19	5	38	0	84	4	94	7	0	1	99	88
Blocks Ranking Size	1	0	0	0	7	1	21	0	45	2	58	2	38	0	63	43
Click Alarmclock	61	5	61	12	63	11	69	41	85	20	83	14	100	38	90	24
Click Bell	54	0	80	9	44	3	54	72	100	35	100	10	100	22	95	43
Dump Bin Bigbin	49	0	64	32	83	24	81	35	91	51	93	28	96	3	92	61
Grab Roller	98	0	74	43	96	80	99	28	99	41	95	57	95	4	100	94
Handover Block	10	0	45	14	45	8	4	0	38	0	81	36	5	0	83	19
Handover Mic	53	0	90	31	98	13	45	0	75	8	96	61	100	0	99	86
Hanging Mug	8	0	23	16	11	3	4	0	12	1	48	5	32	0	46	16
Lift Pot	39	0	72	9	84	36	20	0	87	32	95	34	89	0	100	46
Move Can Pot	39	0	25	12	58	21	48	0	78	0	94	15	85	7	87	24
Move Pillbottle Pad	1	0	8	0	21	1	51	7	92	1	76	26	92	1	90	34
Move Playingcard Away	47	0	43	11	53	22	79	13	92	30	89	53	99	2	98	89
Move Stapler Pad	1	0	2	0	0	2	8	0	27	0	45	19	35	0	24	11
Open Laptop	49	0	59	32	85	46	86	21	96	37	89	37	90	8	94	59
Open Microwave	5	0	37	20	80	50	2	7	0	0	86	24	44	1	50	2
Pick Diverse Bottles	6	0	2	0	27	6	52	18	83	34	76	17	69	4	81	50
Pick Dual Bottles	24	0	42	13	57	12	82	31	93	56	82	30	76	9	93	56
Place A2B Left	2	0	3	1	31	1	74	4	79	12	68	8	76	1	90	69
Place A2B Right	13	0	1	1	27	6	56	1	81	11	52	9	84	3	87	68
Place Bread Basket	14	0	10	2	17	4	63	20	90	29	90	26	96	4	92	71
Place Bread Skillet	11	0	5	1	23	1	71	16	91	26	85	23	85	3	90	60
Place Burger Fries	72	0	50	27	80	4	97	26	99	11	99	37	96	8	90	79
Place Can Basket	18	0	19	6	41	5	20	0	63	0	68	34	58	0	80	44
Place Cans Plasticbox	40	0	6	5	34	2	66	24	94	5	98	47	93	2	99	48
Place Container Plate	41	0	78	17	88	45	86	48	100	58	96	22	98	17	96	86
Place Dual Shoes	8	0	4	4	15	0	45	0	57	0	15	3	24	0	42	24
Place Empty Cup	37	0	56	7	37	11	74	27	97	34	95	28	98	10	92	86
Place Fan	3	0	12	2	20	10	31	1	62	5	62	9	75	1	76	42
Place Mouse Pad	0	0	1	0	7	1	27	0	46	14	51	12	71	0	73	34
Place Object Basket	15	0	33	17	16	2	56	1	66	3	89	25	50	2	93	78
Place Object Scale	1	0	1	0	10	0	36	4	71	0	55	5	80	0	91	53
Place Object Stand	22	0	15	5	36	11	76	24	87	21	84	33	95	12	93	72
Place Phone Stand	13	0	15	6	35	7	32	0	61	2	91	10	85	0	79	52
Place Shoe	23	0	35	7	28	6	76	12	90	29	70	18	83	7	91	79
Press Stapler	6	0	41	24	62	29	79	56	94	58	92	64	58	19	99	45
Put Bottles Dustbin	22	0	21	4	54	13	7	0	42	10	80	13	83	2	93	43
Put Object Cabinet	42	0	33	18	68	18	7	0	52	0	59	8	41	0	45	25
Rotate QRcode	13	0	50	5	68	15	56	2	81	21	69	11	76	0	79	40
Scan Object	9	0	4	1	18	1	47	23	77	32	73	24	77	4	81	59
Shake Bottle Horizontally	59	18	84	51	99	51	100	68	100	73	100	66	100	41	100	97
Shake Bottle	65	8	74	45	97	60	98	54	100	74	98	73	100	49	100	98
Stack Blocks Three	0	0	2	0	17	0	8	0	45	5	96	37	0	0	97	51
Stack Blocks Two	7	0	21	2	42	1	61	0	95	6	100	60	2	0	100	75
Stack Bowls Three	63	0	51	17	66	24	42	1	63	13	92	25	77	1	86	68
Stack Bowls Two	61	0	76	30	91	41	69	12	90	52	98	49	96	11	90	81
Stamp Seal	2	0	1	0	3	4	34	2	77	8	60	21	68	0	73	30
Turn Switch	36	1	35	15	27	23	43	26	49	30	65	27	56	17	62	65
Average	28.0	0.6	34.5	13.7	46.4	16.3	52.9	15.2	75.3	20.5	80.5	26.4	71.9	6.3	84.0	55.7

$t \rightarrow 0$, allowing the low-dimensional action branch to dominate the total objective and disrupt the intended balance with the video loss.

We therefore use a modified x_0 -prediction objective for the action branch, supervising the clean action endpoint directly without the singular $1/t^2$ reweighting. The velocity induced by the predicted endpoint is still used for sampling, but the training signal remains bounded and comparable to the video objective. This preserves the geometric motivation of x_0 -prediction on the locally smooth action manifold while avoiding instability in the joint video-action training regime.

The same motivation also applies to the progress-value token. Rather than treating value as a high-dimensional visual reconstruction signal, MV-WAM introduces it as another low-dimensional manifold variable aligned with the action space. The value token estimates task progress and regulates action generation, providing a compact signal for detecting low-progress action chunks and triggering value-guided rollback.

G Simulation Results

Quantitative results. Table 1 provides the complete per-task RoboTwin 2.0 results corresponding to the summarized benchmark table in the main paper. The full table is included to expose task-level variation that is hidden by the preview table and average success rates. For each task, we report both

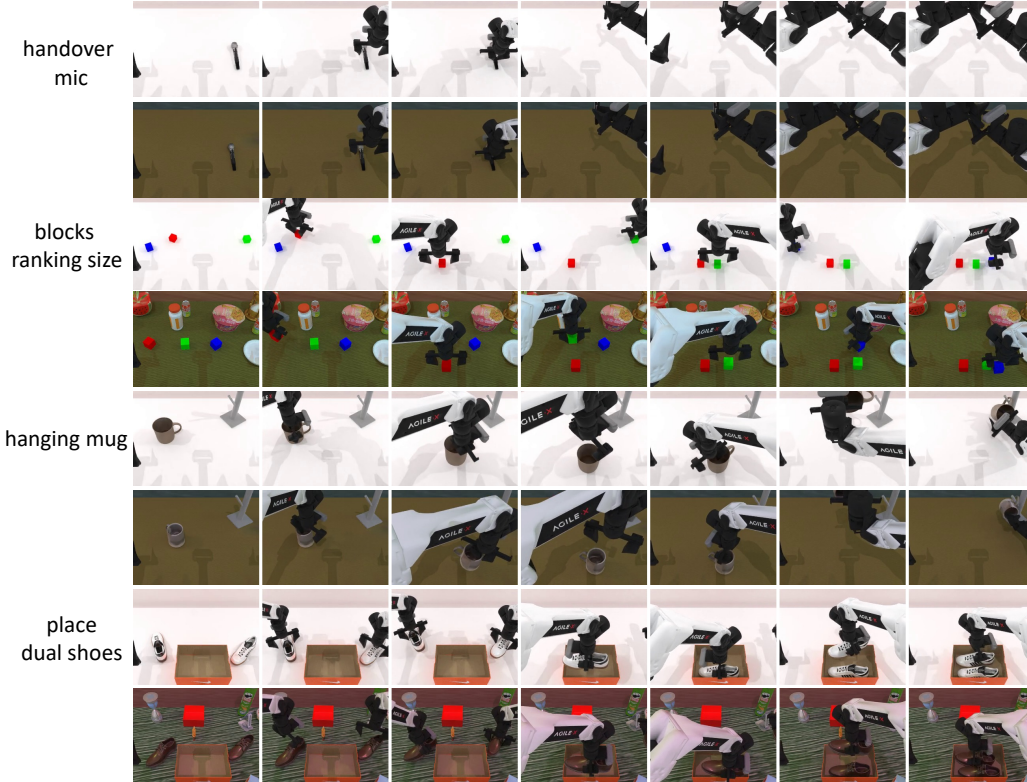


Figure 8: **Robot execution progress in RoboTwin 2.0 simulation tasks.** We visualize key frames of the robot’s execution process from a static exterior view in simulation tasks, including both clean and random scenes.

Clean and Random success rates for all compared VLA and WAM baselines, allowing readers to inspect whether the aggregate trends are consistent across different manipulation categories rather than driven by a small subset of tasks. The complete results show that performance varies substantially across task types. MV-WAM is especially strong on tasks involving visual attribute recognition, spatial placement, and multi-object stacking, such as *Blocks Ranking RGB*, *Place Object Basket*, *Stack Blocks Three*, and *Stack Blocks Two*. The table also reveals remaining difficult cases, including *Open Microwave* and *Move Stapler Pad*, where narrow affordances, contact precision, or unfavorable randomized layouts can still degrade execution. These task-level results complement the main-paper summary by identifying where the proposed model generalizes reliably and where future improvements in local affordance modeling and contact-sensitive control may be most useful.

Qualitative results. In addition to the quantitative results, we provide qualitative rollout visualizations in Fig. 8. These examples illustrate the execution process of MV-WAM under diverse RoboTwin 2.0 tasks and randomized visual conditions. The qualitative results show that MV-WAM can generate temporally consistent action sequences while maintaining stable object interaction across different task categories, including object placement, stacking, and attribute-conditioned manipulation. Notably, the model is able to preserve coherent visual-action alignment under background changes, object layout variations, and distractor objects, which further supports the quantitative improvements observed in the Random setting.

Failure analysis. Although MV-WAM achieves strong overall generalization, we observe two representative failure modes in qualitative rollouts, as illustrated in Fig. 9. The first type of failure is caused by the limited semantic and spatial understanding capacity of the Video Expert. For example, in the *Adjust Bottle* case, the predicted visual rollout captures the general object motion but selects the wrong manipulator: the task should be executed with the left hand, whereas the model incorrectly drives the right hand. This suggests that the visual imagination branch can still produce plausible but semantically misaligned futures when the task requires fine-grained reasoning about

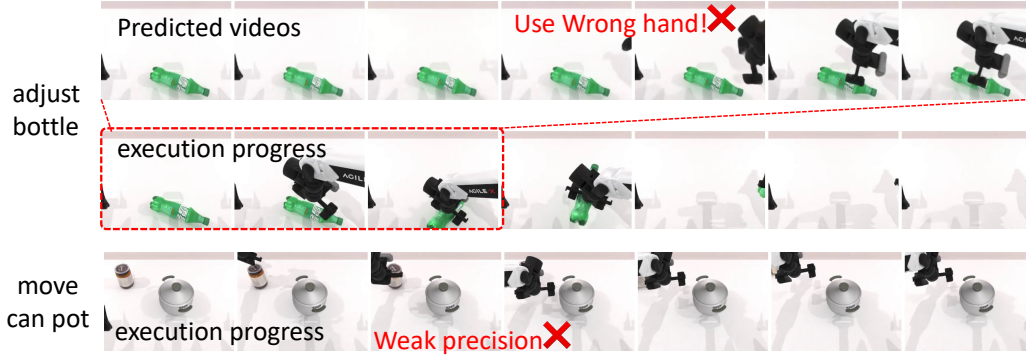


Figure 9: Wrong Robot execution progress in RoboTwin2.0 simulation tasks.

arm assignment, object-side relations, or embodiment-specific constraints. The second type of failure comes from insufficient action precision in contact-sensitive scenarios. In the *Move Can Pot* case, the model predicts a generally correct interaction direction, but the generated action trajectory lacks the fine-grained positional accuracy required for successful execution. Such errors often appear when the task involves small affordances, narrow contact regions, or precise end-effector alignment. These observations indicate that future improvements should strengthen both high-level visual understanding for embodiment-aware planning and low-level action accuracy for fine-grained contact control.

H Broader Impact

MV-WAM studies more robust and generalizable robotic manipulation by improving how robot policies adapt to diverse visual conditions and execution scenarios. Such systems have the potential to improve productivity and quality of life by assisting with repetitive, physically demanding, or hazardous tasks in domains such as manufacturing, logistics, healthcare support, and domestic service. More generalizable manipulation policies may also reduce the engineering cost required to adapt robots to new environments, making robotic assistance more accessible across diverse real-world settings.

At the same time, deploying capable manipulation systems raises important safety and societal concerns. Robots operating in open environments may cause unintended physical damage or safety risks when facing unfamiliar objects, humans, or environmental conditions. Large-scale deployment could also affect labor markets by automating certain manual tasks and may introduce accountability challenges when failures occur. Therefore, systems such as MV-WAM should be deployed only with rigorous safety evaluation, human oversight, clear operational boundaries, and mechanisms for monitoring and intervention. Future work should continue to study robustness, failure modes, and safe human-robot interaction before real-world deployment.